






# Binarity and Accretion in AGB Stars: *HST*/*STIS* Observations of UV Flickering in Y Gem

R. Sahai<sup>1</sup> , C. Sánchez Contreras<sup>2</sup> , A. S. Mangan<sup>1,3</sup>, J. Sanz-Forcada<sup>2</sup> , C. Muthumariappan<sup>4</sup>, and M. J. Claussen<sup>5</sup>

<sup>1</sup>Jet Propulsion Laboratory, MS 183-900, California Institute of Technology, Pasadena, CA 91109, USA

<sup>2</sup>Astrobiology Center (CSIC-INTA), ESAC Campus, E-28691 Villanueva de la Cañada, Madrid, Spain

<sup>3</sup>Iowa State University, Ames, IA 50011, USA

<sup>4</sup>Indian Institute of Astrophysics, Bangalore 560034, India

<sup>5</sup>National Radio Astronomy Observatory, 1003 Lopezville Road, Socorro, NM 87801, USA

Received 2018 February 22; revised 2018 May 6; accepted 2018 May 8; published 2018 June 18

## Abstract

Binarity is believed to dramatically affect the history and geometry of mass loss in AGB and post-AGB stars, but observational evidence of binarity is sorely lacking. As part of a project to search for hot binary companions to cool AGB stars using the *GALEX* archive, we discovered a late-M star, Y Gem, to be a source of strong and variable UV and X-ray emission. Here we report UV spectroscopic observations of Y Gem obtained with the *Hubble Space Telescope* that show strong flickering in the UV continuum on timescales of  $\lesssim 20$  s, characteristic of an active accretion disk. Several UV lines with P-Cygni-type profiles from species such as Si IV and C IV are also observed, with emission and absorption features that are red- and blueshifted by velocities of  $\sim 500$  km s<sup>-1</sup> from the systemic velocity. Our model for these (and previous) observations is that material from the primary star is gravitationally captured by a companion, producing a hot accretion disk. The latter powers a fast outflow that produces blueshifted features due to the absorption of UV continuum emitted by the disk, whereas the redshifted emission features arise in heated infalling material from the primary. The outflow velocities support a previous inference by Sahai et al. that Y Gem's companion is a low-mass main-sequence star. Blackbody fitting of the UV continuum implies an accretion luminosity of about  $13 L_{\odot}$ , and thus a mass-accretion rate  $> 5 \times 10^{-7} M_{\odot} \text{ yr}^{-1}$ ; we infer that Roche-lobe overflow is the most likely binary accretion mode for Y Gem.

**Key words:** binaries: close – circumstellar matter – stars: AGB and post-AGB – stars: individual (Y Gem) – stars: mass-loss

## 1. Introduction

One of the biggest challenges for 21st century stellar astronomy is a comprehensive understanding of the impact of binary interactions on stellar evolution. Close binary interactions are expected to dominate a substantial fraction of stellar phenomenology—e.g., cataclysmic variables, SNe Ia progenitors, and low- and high-mass X-ray binaries.

Binary star interactions are specifically believed to underlie the formation of the overwhelming majority of planetary nebulae (PNe), which represent the bright end stage of most stars in the universe. Such interactions are likely the key to the resolution of this long-standing puzzle: although PNe (and their progenitors, pre-PNe [PPNe]) evolve from slowly expanding ( $V_{\text{exp}} \sim 5\text{--}15$  km s<sup>-1</sup>), spherically symmetric circumstellar envelopes of AGB stars, modern surveys reveal that the vast majority of the former deviate strongly from spherical symmetry, showing a dazzling variety of elliptical, bipolar, and multipolar morphologies and fast, collimated outflows ( $V_{\text{exp}} \gtrsim 50\text{--}100$  km s<sup>-1</sup>; e.g., Sahai & Trauger 1998; Balick & Frank 2002; Sahai et al. 2011a).

A close association between jets and binary interaction involving a red giant or AGB primary is exemplified by symbiotic stars, a small class of objects in which the optical spectrum shows features of TiO (showing the presence of a cool red giant primary), but also optical emission lines, e.g., H I, He II, and [O III]. In such objects, a compact star, usually a white dwarf (WD), accretes matter from the giant primary. Prime examples of symbiotic stars with jets are R Aqr and CH Cyg (e.g., Corradi et al. 1999).

However, there is a lack of observational evidence of widespread binarity in AGB stars. We have therefore been using UV and X-ray observations as new probes of accretion-related phenomena in AGB stars—archival surveys in the UV using the *GALEX* database show that a large fraction of AGB stars show FUV emission, with relatively high FUV/NUV flux ratios and significant variability, likely resulting from variable accretion associated with a companion (Sahai et al. 2008, 2011b, 2015, 2016). Roughly, about 40% of objects surveyed show strong, variable, X-ray emission that likely arises in an accretion disk around a compact companion (see Sahai et al. 2015, hereafter Setal15). In this paper, we report stochastic variations on  $\lesssim 20$  s timescales in the UV spectrum of our best-studied UV-/X-ray-emitting star, Y Gem, similar to the flickering phenomenon seen in other well-known classes of accreting binaries. These variations provide independent and robust evidence of binarity in this object.

Until recently, Y Gem lacked a significant measurement of the parallax (its *Hipparcos* parallax/error is 1.30 mas/1.38 mas: van Leeuwen 2007), and we have adopted, in our previous studies of this object, a distance of  $D = 0.58$  kpc, as inferred from its *K*-band magnitude, following Kahane & Jura (1994) who assume that late-M semi-regular stars have absolute magnitudes  $M_K = -7.6$  (Sahai et al. 2011b; Setal11). In the recent *Gaia* Data Release 2 (L. Lindegren et al. 2018, in preparation), its measured parallax is  $1.4997 \pm 0.1561$  mas, giving a distance of  $0.67 \pm 0.07$  kpc. Since this is roughly within  $1\sigma$  of our adopted value, we have conservatively kept our original distance estimate for this paper, especially since the DR2 results have yet to be subjected to scrutiny by the

**Table 1**  
Log of Observations

Data Set	Exp. # <sup>a</sup>	Grating	Start Time	Exp.Time <sup>b</sup>
OD9C01010	10	G140L	2016-10-11 21:56:34	347.020
OD9C01020	20	G140L	2016-10-11 22:05:47	347.020
OD9C01030	30	G230L	2016-10-11 23:02:57	312.126
OD9C01040	40	G230L	2016-10-11 23:12:10	304.769
OD9C01050	50	G140L	2016-10-11 23:26:06	517.020
OD9C01060	60	G140L	2016-10-11 23:38:09	517.020
OD9C01070	70	G230L	2016-10-12 00:38:23	503.600
OD9C01080	80	G230L	2016-10-12 00:50:26	486.315

**Notes.**

<sup>a</sup> Exposure No.

<sup>b</sup> Exposure Time (s).

astrophysical community. The slightly larger distance, if correct, would imply a  $\sim 30\%$  increase in estimated luminosities and does not affect our conclusions.

The plan of this paper is as follows. We describe the observational setup in Section 2, and the data reduction and calibration procedures in Section 3. The observational results and their analysis are described in Section 4, with a focus on the spectral time variability (Section 4.1), the UV continuum and its modeling (Section 4.2), and the line profiles (Section 4.3). We present a new geometrical model to explain our results and discuss their implications for binarity and accretion in Y Gem in Section 5. Our main conclusions are summarized in Section 6.

## 2. Observations

We obtained UV spectra of Y Gem with the Space Telescope Imaging Spectrograph (STIS) on board the *Hubble Space Telescope* (HST) between UT 22:05 10-11-2016 and 00:47 10-12-2016, using the G140L and G230L gratings, and the  $52'' \times 0.2''$  aperture in Time-Tag mode. The slit width fully encompasses the entire source, which is expected to be unresolved (Setal15). The observing sequence consisted of two pairs of G140L exposures followed by two pairs of G2300L exposures; this sequence was repeated a second time, providing four separate exposures each in the two wavelength bands ( $\sim 1120\text{--}1700 \text{ \AA}$  and  $\sim 1600\text{--}3150 \text{ \AA}$ ). An observation log is given in Table 1. We obtained similar data during a following epoch (2017 April), but during these observations the source was much brighter, causing the Time-tag buffer to overflow, so the absolute flux levels are not reliable. These data will be discussed in a subsequent paper.

## 3. Data Reduction

In order to observe changes in the spectra over time intervals smaller than the full integration time of each exposure, we analyzed our data in Time-Tag mode, following the procedure described in the STIS Time-Tag Analysis Guide (Dashevsky et al. 2000). We used IRAF to run the “odelaytime” command, which applied heliocentric and barycentric time corrections, followed by “inttag,” which created a raw data file, with multiple subexposures of a chosen duration. Each subexposure used data only in the good time intervals (GTIs). The subexposures at the end of each GTI had shorter durations resulting in relatively larger errors in the associated fluxes. In our analysis below, we chose a subexposure time of 20 s in

order to obtain a good signal-to-noise ratio while still maintaining a large number of subexposures for our timing analysis. We ran calstis in PyRAF to create FITS-format files of the calibrated subexposure data.

## 4. Results and Analysis

The G140L and G230L spectra show the presence of continuum emission and many strong emission lines, some with blueshifted absorption features resulting in P-Cygni-type profiles (e.g., Castor 1970), from ionized levels of abundant metals such as C, O, N, Si, and Mg. No molecular H<sub>2</sub> lines are seen. Representative spectra and line lists are given in Figures 1 (a) and (b) and Table 2, respectively. For both the subexposure and full exposure spectra, we used small line-free wavelength windows around each strong line feature to subtract an underlying linear continuum, followed by Gaussian line fitting to determine the line center, the FWHM, and the flux of the emission and absorption features (e.g., Figure 1(c)). The instrumental resolution, which varies from 1.7 (2.2) to 1.4 (2.1) $\text{\AA}$  over the wavelength range of the G140L (G230L) grating, has been deconvolved from the line-width values in Table 2. Representative line fitting results are given for exposures 20 and 30 in Table 2.

### 4.1. Time Variations

Our analysis of the subexposure spectra reveals fast variations in the continuum UV flux of Y Gem at all wavelengths (Figures 2(a) and (d)). The continuum light curves, extracted from line-free regions, and that underlying the different spectral lines, are quite similar, with significant variations seen across successive subexposures, implying variability on timescales of 20 s or less. The maximum peak-to-peak amplitude of the continuum variations is 0.53 mag (exposure 60). Using the ratio between the observed and expected root-mean-square variability ( $s$  and  $s_{\text{exp}}$ , respectively) to quantify the significance of stochastic variations in the light curves (see e.g., Nuñez et al. 2016), we find  $s/s_{\text{exp}} \sim 6\text{--}8$  for several line-free continuum windows in the G140L and G230L spectra. Periodogram analysis reveals no specific period; the variations appear to be stochastic in nature.

Fluctuations in the spectral-line parameters are also seen, but the uncertainties in the fitted parameters are larger and so in general, the variability is less significant than in the continuum. However, we do find significant fractional variations in the Si IV(1) absorption line equivalent width (Figure 2(b)) and in the Si IV(1) absorption and emission-line Doppler shifts (Figure 2(c)). In addition, the amplitude of the blueshift for the Si IV(1) absorption feature appears to be anticorrelated with the redshift of the Si IV(1) emission feature. In contrast, the Si IV(1) and C IV(1,2) emission-line fluxes show much smaller variations within each exposure.

During the period covering exposures 10–60 ( $\sim 1.7$  hr), excluding that covered by exposure 50, we find a general decline in the continuum fluxes and the Si IV(1) absorption equivalent width and blueshift; however, these, together with the continuum fluxes, all deviate upward from the above trend during exposure 50. The most striking decline (by factors  $>5$ ) is seen in the Si IV(1) equivalent width, from the end of exposure 50 to the end of exposure 60. Correspondingly, the FUV continuum declines to its lowest level in exposure 60. The Si IV(1) absorption line equivalent width shows a broad peak at

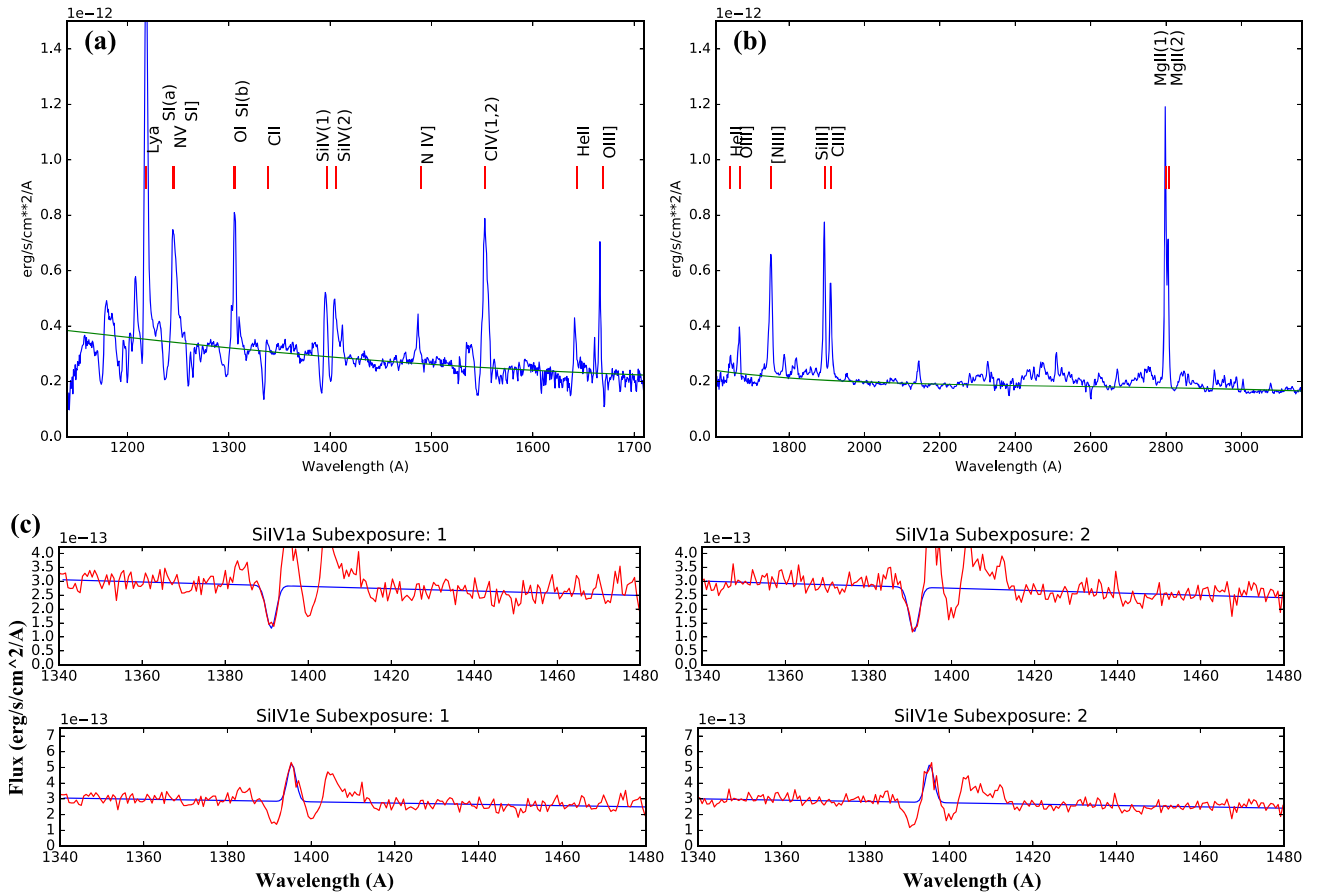


**Figure 1.** Representative STIS/UV spectra of Y Gem observed using gratings (a) G140L (exposure 20) and (b) G230L (exposure 30). Exposures 20 and 30 were used to calculate the parameters for the spectral lines in Table 2. The green curves show a model fit consisting of two blackbody components, characterized by  $T_{\text{eff}} = 35,500$  K,  $L = 6.3 L_{\odot}$ , and  $T_{\text{eff}} = 9400$  K,  $L = 6.7 L_{\odot}$ . (c) STIS/UV spectra of Y Gem in the vicinity of the Si IV(1) line for the first two 20 s subexposure in exposure 20. The blue curve shows Gaussian line-profile fits (together with a linear baseline) to the absorption (top) and emission (bottom) features. Such fitting has been used to calculate the parameters for the spectral lines in Table 2.

an epoch that lies between the two peak luminosity epochs in exposure 50. We interpret these correlations in the context of a geometric model in Section 5.

We note that much smaller amplitude photometric variations have been recently reported at optical wavelengths (e.g., 0.06 mag peak to peak in the  $u'$  band with a typical timescale of 10 minutes) for Y Gem using ground-based differential photometry (Snaid et al. 2018). Although a comparison with differential photometry of two field stars indicates that these variations are significant, the effects of aperture photometry in variable seeing conditions can produce spurious fluctuations that are not easily quantified. For example, in the Snaid et al. data set, large spurious fluctuations are clearly noticeable in both the differential photometry and the seeing  $\sim 10$ – $20$  minutes into the observation time stream, but smaller seeing fluctuations are present in the remainder of the time stream and may be contributing to the photometric variations as well.

#### 4.2. Continuum Modeling

Single-blackbody fits (using least-squares minimization) to the G140L spectra from exposures 10, 20, 50, and 60 give values for the luminosities of  $L \sim 6.9$ , 6.0, 6.4, and  $4.5 L_{\odot}$  and effective temperatures of  $T_{\text{eff}} \sim 31,440$ , 29,600, 29,540, and 29,980 K, respectively. However, these blackbodies do not provide sufficient flux at the longer wavelengths (i.e.,  $\gtrsim 1800$  Å)

covered in the G230L spectra; a significantly cooler blackbody is needed to fit the latter. For example, single-blackbody fits to the G230L spectra from exposures 30, 40, 70, and 80 give values for the luminosities of  $L \sim 7.0$ , 7.0, 4.9, and  $5.5 L_{\odot}$  and effective temperatures of  $T_{\text{eff}} \sim 13,140$ , 13,800, 13,400, and 13,450 K, respectively. Thus, whereas the effective temperatures do not change much with time, the luminosities derived for both the hotter and cooler blackbodies above show significant changes that are similar to those seen in the continuum level in the G140L and G230L exposures. We have not included dust extinction in our modeling because there is no measurable dust excess in Y Gem (Setal11).

In order to constrain the values of  $L$  and  $T_{\text{eff}}$  for each of these blackbodies and their variations more accurately, we construct a model that combines two blackbodies to fit the G140L and G230L spectra. Since the G140L and G230L spectra are not co-eval, and the fits above indicate that both  $L$  and  $T_{\text{eff}}$  can vary with time, we use exposures 40 (for G230L) and 50 (for G140L) as these were taken closest to each other in time. We find that the G140L spectrum requires  $L(h) = 6.8 L_{\odot}$  and  $T_{\text{eff}}(h) \sim 36,600$  K, and a cooler blackbody with  $L(c) \sim 6.3 L_{\odot}$  and  $T_{\text{eff}}(c) \sim 9940$  K. Thus,  $L(h)$  and  $T_{\text{eff}}(h)$  respectively increase by about 6% and 24%, and  $L(c)$  and  $T_{\text{eff}}(c)$  respectively decrease by about 29% and 24%, over the corresponding single-blackbody fits. The two-blackbody fits for the other pairs of successive G140L+G230L exposures

**Table 2**  
Properties of Selected Observed Lines from Exposures 20 (G140L) and 30 (G230L)

Name	Rest $\lambda$ ( $\text{\AA}$ )	Emiss./Abs. <sup>a</sup>	Obs. $\lambda$ ( $\text{\AA}$ )	$V_{\text{hel}}$ ( $\text{km s}^{-1}$ )	FWHM <sup>b</sup> ( $\text{km s}^{-1}$ )	Flux ( $10^{-13}$ ergs $\text{cm}^{-2}$ $\text{s}^{-2}$ )
Ly $\alpha$	1215.670	Emiss.	1218.573 $\pm$ 0.008	716 $\pm$ 2	774 $\pm$ 4	54.5 $\pm$ 0.4
Si IV(1) <sup>c</sup>	1393.756	Abs.	1391.200 $\pm$ 0.030	-549 $\pm$ 7	565 $\pm$ 17	-4.70 $\pm$ 0.15
Si IV(1) <sup>c</sup>	1393.756	Emiss.	1395.657 $\pm$ 0.023	409 $\pm$ 5	436 $\pm$ 11	6.84 $\pm$ 0.19
Si IV(2) <sup>d</sup>	1402.770	Abs.	1400.366 $\pm$ 0.037	-514 $\pm$ 8	322 $\pm$ 19	-2.43 $\pm$ 0.13
Si IV(2) <sup>d</sup>	1402.770	Emiss.	1404.613 $\pm$ 0.030	394 $\pm$ 6	518 $\pm$ 16	6.73 $\pm$ 0.23
C IV(1,2) <sup>e</sup>	1549.490	Emiss.	1553.249 $\pm$ 0.026	727 $\pm$ 5	941 $\pm$ 11	27.7 $\pm$ 0.5
C IV(1,2) <sup>e</sup>	1549.490	Abs.	1545.309 $\pm$ 0.060	-809 $\pm$ 12	588 $\pm$ 30	-3.42 $\pm$ 0.21
Si III]	1892.030	Emiss.	1893.453 $\pm$ 0.026	225 $\pm$ 4	915 $\pm$ 9	34.5 $\pm$ 0.5
C III] <sup>f</sup>	1908.734	Emiss.	1910.320 $\pm$ 0.038	249 $\pm$ 6	1022 $\pm$ 14	23.4 $\pm$ 0.4
Mg II(1) <sup>c</sup>	2796.352	Emiss.	2798.318 $\pm$ 0.013	211 $\pm$ 1	537 $\pm$ 3	49.8 $\pm$ 0.4
Mg II(2) <sup>d</sup>	2803.531	Emiss.	2804.983 $\pm$ 0.033	155 $\pm$ 4	511 $\pm$ 7	27.8 $\pm$ 0.4

#### Notes.

<sup>a</sup> Emiss.—Emission, Abs.—Absorption.

<sup>b</sup> Corrected for instrumental resolution.

<sup>c</sup> First line in a resolved (or partially resolved) doublet.

<sup>d</sup> Second line in a resolved (or partially resolved) doublet.

<sup>e</sup> Mean wavelength of unresolved C IV doublet with  $\lambda_0 = 1548.20$   $\text{\AA}$  and  $1550.78$   $\text{\AA}$ .

<sup>f</sup> Unresolved blend with [C III] transition at  $\lambda_0 = 1906.683$   $\text{\AA}$ .

(20+30 or 60+70) produce very similar values of  $L(h)$ ,  $T_{\text{eff}}(h)$ ,  $L(c)$ , and  $T_{\text{eff}}(c)$ , but these are much more uncertain as the G140L+G230L exposure pairs have very long time gaps between them (about 1 hr).

We investigate luminosity and temperature changes in both blackbodies on the short variability timescales that we find for the continuum, as follows. First, we determine  $L(h)$  and  $T_{\text{eff}}(h)$  as a function of subexposure in exposure 50 using two-blackbody fits, with  $L(c)$  and  $T_{\text{eff}}(c)$  set to their (average) values for exposure 40 (as determined above). Then, in order to account for the variability of  $L(c)$  and  $T_{\text{eff}}(c)$  during exposure 50, we follow the following procedure. First, using a single-blackbody fit to the subexposure spectra in exposure 40, we find that the peak-to-peak variations in  $L(c)$  and  $T_{\text{eff}}(c)$  are about  $\pm 10\%$  and  $\pm 3\%$ , respectively. Using these to set upper and lower bounds on the average value of  $L(c)$  and  $T_{\text{eff}}(c)$ , we determine the upper and lower bounds on the variability of  $L(h)$  and  $T_{\text{eff}}(h)$ . We find significant variations in  $L(h)$  (Figure 2(e)), but not in  $T_{\text{eff}}(h)$ . A similar analysis for the cooler blackbody shows that the variations in  $L(c)$  are marginally significant (Figure 2(f)), and no significant variations are found for  $T_{\text{eff}}(c)$ . The variations in  $L(h)$  and  $L(c)$  follow the variations in the continuum fluxes (Figures 2(e) and (f)).

#### 4.3. Line Profiles

All emission lines are redshifted relative to the systemic velocity ( $V_{\text{hel}} = 13.5$   $\text{km s}^{-1}$ ); the velocities lie in the range  $V_{\text{hel}} \sim 400$ – $700$  ( $150$ – $250$ )  $\text{km s}^{-1}$  for lines observed with the G140L (G230L) grating (Table 2, Figure 3). Prominent P-Cygni-type absorption features are seen in lines of NV, O I, Si IV, and C IV. The blueshifted absorption features in these profiles are consistent with the presence of a high-speed outflow ( $>500$   $\text{km s}^{-1}$ ) along the line of sight (los) to a hot continuum source. The lack of absorption features in semi-forbidden lines such as Si III] $\lambda$  1892.03 and C III] $\lambda$  1908.73 is probably due to these being excited in a low-density region that is much larger than the continuum source.

But the large values of the redshifts of the emission features<sup>6</sup> ( $V_{\text{red}}(e)$ ) are discrepant from our expectation for a classical P-Cygni profile that results from an outflow surrounding a continuum source—in these profiles, the emission feature is generally centered near or at the systemic velocity (Castor 1970). However, if the outflow velocity distribution covers values over a range from  $\sim 0$  to  $V_{\text{max}}$  and there is substantial line broadening, e.g., due to microturbulence, the absorption feature may be wide enough to extend to redshifted velocities, thereby reducing the emission feature’s blue-wing intensity and thus shifting its centroid substantially redwards of the systemic velocity. But, as can be seen in the predicted spectra from detailed P-Cygni models by van Loon et al. (2001, hereafter vLKH01), it is only when the absorption feature is extremely saturated, and the microturbulence is a substantial fraction of the maximum outflow velocity ( $V_{\text{max}}$ ), that one gets values of  $V_{\text{red}}(e)$  comparable to the blueshift of the absorption feature, which is located at or near  $-V_{\text{max}}$  (e.g., see Figure 9(a) of vLKH01, where  $\tau = 300$  and the line-broadening parameter  $\sigma_v = 0.45$ ).<sup>7</sup> When the lines are less optically thick,  $V_{\text{red}}(e)$  is about 0.3–0.5 for  $\tau = 10$ – $100$  (e.g., see Figure 6(a), (b) of vLKH01, where  $\sigma_v = 0.2$ ). Since the observed absorption features in our spectra are clearly not heavily saturated, we conclude that a classical P-Cygni model can probably not explain Y Gem’s UV lines.

Another model to explain P-Cygni profiles is one that was proposed for the PPN Hen 3–1475 (Sánchez Contreras & Sahai 2001) to explain its H $\alpha$  profile (observed with *HST*/STIS), which also shows blueshifted (redshifted) absorption (emission) features. This model features a fast, neutral, collimated outflow within more slowly expanding bipolar lobes with dense, dusty walls. H $\alpha$  photons produced from a central source pass through gas in the collimated outflow producing the absorption feature and then are scattered from the dusty walls along the los, producing a redshifted emission feature. However, unlike Hen 3–1475, there is

<sup>6</sup> As a fraction of the outflow velocity.

<sup>7</sup> In these and other plots of model spectra in vLKH01, all velocities are given as a fraction of  $V_{\text{max}}$ , which is set to 1.



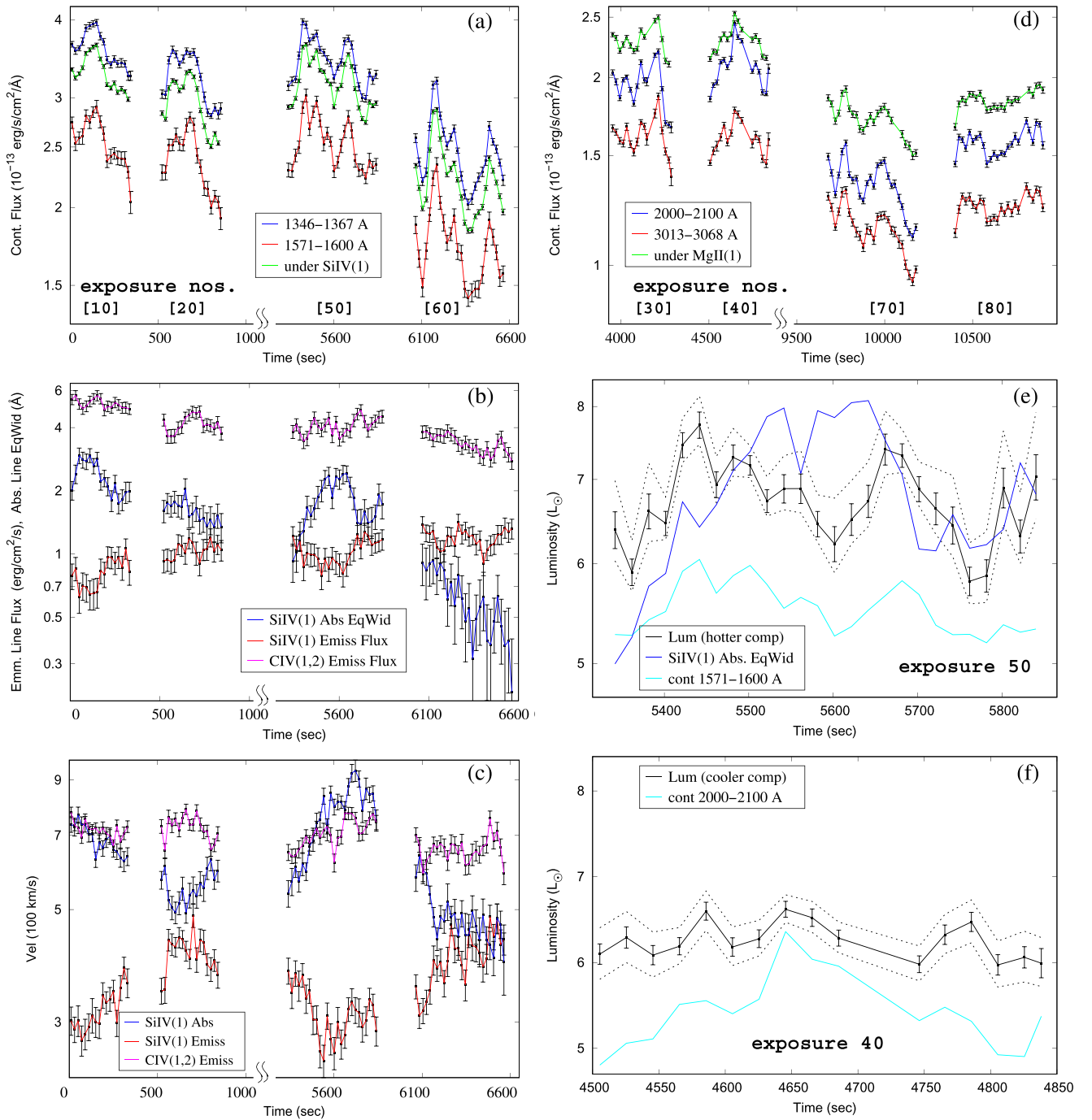


**Figure 2.** Short-term time variations in the continuum and lines observed in Y Gem: (a) line-free continuum in the bands 1346–1367 Å (blue) and 1571–1600 Å (red), and continuum underlying the Si IV(1) line (green). (b) The equivalent width of the Si IV(1) absorption line (blue) and the flux of the Si IV(1) (red) and C IV(1, 2) emission lines (pink). The emission-line fluxes have been scaled up by a factor of  $1.5 \times 10^{12}$ . (c) The Doppler shifts (absolute values) of the lines in panel (b): the Si IV(1) absorption feature is blueshifted, whereas the Si IV(1) and C IV(1, 2) emission features are redshifted. (d) The line-free continuum in the bands 2000–2100 Å (blue) and 3013–3068 Å (red), and the continuum underlying the Mg II(1) line (green; scaled up by a factor of 1.1 for clarity). Error bars in panels (a)–(d) are  $\pm 1\sigma$ . The light curves in panels (a)–(c) and (d) are, respectively, extracted from the G140L exposures 10, 20, 50, and 60 and G230L exposures 30, 40, 70, and 80. (e) The hotter blackbody’s luminosity (black), derived using a two-blackbody fit to the continuum observed in the subexposures within exposure 50: the dashed curves show the upper and lower bounds on the luminosity due to the estimated uncertainties in the cooler blackbody’s luminosity and temperature. The 1571–1600 Å continuum, scaled up by a factor of  $1.1 \times 10^7$  (cyan), and the square root of the Si IV(1) absorption line equivalent width, scaled up by a factor of 5.2 (blue), are shown for comparison. (f) As in panel (e), but for the cooler blackbody’s luminosity, derived from fitting the subexposures within exposure 40 (the 2000–2100 Å continuum, scaled up by a factor of  $2.6 \times 10^{13}$  (cyan), is shown for comparison).

no measurable dust excess in Y Gem (Setal11), so the presence of dusty lobes in it is somewhat implausible.

We propose below a new geometric model to explain the large values of  $V_{\text{red}}(e)$ .

## 5. Discussion

The short-term stochastic fluctuations in the UV continuum of Y Gem appear to be similar to the photometric variations seen in other well-known classes of accreting binaries,

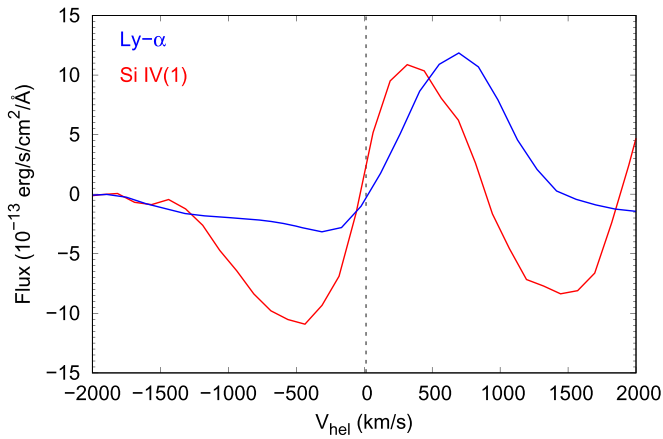


**Figure 3.** Ly $\alpha$  (blue) and Si IV(1) (red) line profiles (continuum-subtracted) from exposure 20. The dashed vertical line shows the systemic velocity.

commonly labelled as “flickering”—e.g., cataclysmic variables and recurrent novae (e.g., Bruch 2015), X-ray binaries with neutron stars and black holes (e.g., van der Klis 2006), symbiotic stars (e.g., Zamanov et al. 2017), and active galactic nuclei (e.g., Pronik et al. 1999). The timescale of flickering depends on the dimensions of the region where the emission arises.

Using the light-travel time corresponding to  $\lesssim 20$  s, characteristic of the variations that we have found in Y Gem, we estimate that the continuum-emitting region is less than  $\sim 0.05$  au ( $8.6 R_{\odot}$ ) in size. Our previous X-ray and UV observations of Y Gem also show variability, including both a quasi-periodic and a stochastic component (Setal15). The periodic component seen most clearly in the X-ray data has  $P \sim 1.3$  hr, which Setal15 interpreted as being associated with emission from the inner radius of an accretion disk around a subsolar mass ( $\lesssim 0.35 M_{\odot}$ ) main-sequence (MS) companion, although a cold ( $T_{\text{eff}} < 30,000$  K) WD could not be excluded.<sup>8</sup>

However, the bulk outflow speed implied by the velocity offset (from the systemic velocity) of the absorption features ( $\sim 500$  km s $^{-1}$ ) strongly argues for a main-sequence companion. On both theoretical and empirical grounds, the speed of an outflow driven from an accretion disk is expected to be of the order of the escape velocity close to the central accreting object (Livio 1997),  $V_{\text{esc}} = 620$  km s $^{-1}$  ( $M_c/R_c$ ) $^{0.5}$ , where  $M_c$  and  $R_c$  are the companion mass and radius in solar units. Thus, the observed bulk expansion velocity of the high-speed outflow is consistent with a solar or subsolar MS companion—e.g., if  $M_c \sim 0.35 M_{\odot}$  (thus,  $R_c = 0.44 R_{\odot}$ : inferred using Table 15.8 in Cox 2000), which is the largest companion mass allowed by the 1.3 hr orbital period seen in Y Gem’s X-ray light curve (Setal15), then  $V_{\text{esc}} = 550$  km s $^{-1}$ . For a cool WD, with a typical mass of  $0.6 M_{\odot}$  and radius of  $0.01 R_{\odot}$ ,  $V_{\text{esc}} = 4800$  km s $^{-1}$  ( $M_c/0.6$ ) $^{0.5}$  ( $0.01/R_c$ ) $^{0.5}$  is much larger than the observed outflow velocities. Any correction to the outflow velocity due to projection effects is likely to be small, given our geometrical model for the continuum source and outflow (described later in this section).

Neither of the two blackbodies discussed in Section 4.2 fit the properties of a viable stellar companion to the primary. The hotter blackbody is overluminous compared to the expected

value for a cool WD ( $T_{\text{eff}} \sim 36,500$  K,  $L < 0.5 L_{\odot}$ ; Figure 8 of Miller Bertolami 2016). The cooler blackbody is underluminous for a main-sequence star ( $T_{\text{eff}} \sim 9400$  K, i.e., spectral type early-A,  $L \sim 30\text{--}80 L_{\odot}$ ). Note, of course, that neither of these blackbodies is consistent with the temperature and luminosity of a  $0.35 M_{\odot}$  main-sequence companion. We conclude that both the hot and cool UV components arise in the accretion disk.

Assuming that the combined luminosity of the hot and cool blackbodies results from accretion, i.e.,  $L_{\text{acc}} = 13 L_{\odot}$  during exposures 40–50, then taking  $L_{\text{acc}} \lesssim \dot{M}_{\text{acc}} M_c / R_c$ , where  $\dot{M}_{\text{acc}}$  is the accretion rate, and  $M_c \sim 0.35 M_{\odot}$  and  $R_c = 0.44 R_{\odot}$  (as above), we find that  $\dot{M}_{\text{acc}} > 5 \times 10^{-7} M_{\odot} \text{ yr}^{-1}$ . This relatively large accretion rate makes wind-accretion mechanisms such as Bondi–Hoyle or wind Roche-lobe overflow (e.g., Huarte-Espinosa et al. 2013; Chen et al. 2017) infeasible because Y Gem does not have a detectable wind—the very weak, narrow CO  $J = 2\text{--}1$  emission line detected toward it likely arises in an extended disk (Setal11), and the infrared excess is negligible or very low (McDonald et al. 2012), implying a mass-loss rate of  $\lesssim 10^{-7} M_{\odot} \text{ yr}^{-1}$  (Snaid et al. 2018). Therefore, either the primary overflows its Roche lobe and transfers material to the accreting star, or accretion occurs within a common-envelope (CE) configuration. For these two accretion modes, the binary separation must be small enough and comparable to the primary star’s radius—1.5 au for Y Gem’s luminosity and effective temperature of 5800  $L_{\odot}$  and 2800 K, respectively (Setal11). However, since we observe the accretion luminosity in the UV, a CE scenario—in which the radiation would be trapped within the envelope—is less likely. We conclude that Roche-lobe overflow is the most likely accretion mode for Y Gem.

The absence of molecular H $_2$  lines (e.g., prominently detected in accreting T Tauri stars: Ingleby et al. 2011) in Y Gem’s UV spectrum is striking, especially since the detection of the 6.4 keV Fe I line in its X-ray spectrum implies the presence of a neutral disk in it. The two main mechanisms for exciting H $_2$  lines are fluorescence due to Ly $\alpha$  pumping (e.g., Yang et al. 2011) or collisional excitation by hot electrons (e.g., Ingleby et al. 2009). If the disk in Y Gem is composed primarily of molecular gas, then the absence of the H $_2$  lines suggests that there are large temporal variations in the total amount of neutral material in the disk. Alternatively, H $_2$  line emission could be present but blocked from the observer’s view by an optically thick continuum-emitting region of hot gas. Otherwise, the disk is primarily composed of atomic gas.

We propose a simple geometric model that can explain the Doppler shifts of the absorption and emission features (Figure 4). In this model, material from the primary AGB star (either from an outflow or Roche-lobe overflow) is gravitationally focused toward the companion, producing a hot accretion disk. The emission features arise in the infalling material, which gets heated either from internal shocks (e.g., due to density and velocity variations within the stream) and/or friction due to passage through the accretion disk’s “atmosphere.” The accretion disk produces an outflow that is seen in absorption against the continuum emission from the accretion disk. Sufficiently hot regions in the disk may also produce UV emission lines, which would be centered roughly around the systemic velocity. Since we do not see a signature of such emission in our spectra, the disk emission lines must be relatively faint compared to those from the outflow, and the

<sup>8</sup> A hot WD (as in symbiotic stars) is ruled out by Setal15 because no optical forbidden line emission—characteristic of symbiotic star spectra—is seen in Y Gem’s M8 optical spectrum.

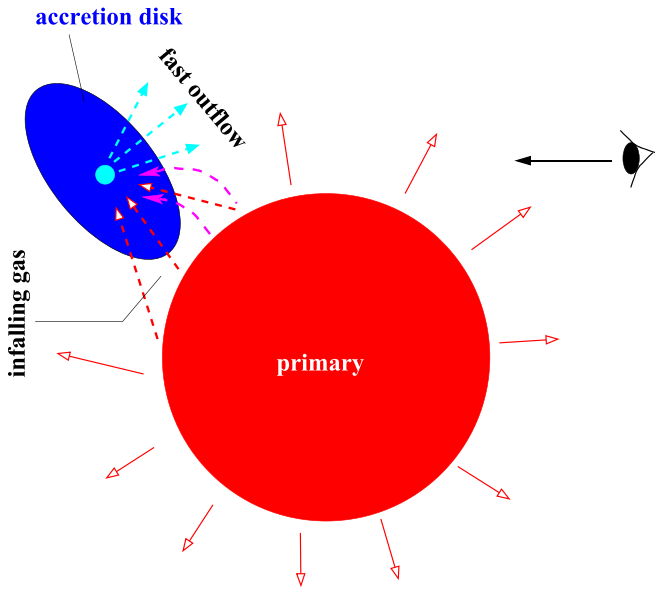


**Figure 4.** Schematic geometry of a model (not to scale) to explain the Doppler shifts of the absorption and emission features observed in the UV spectra of Y Gem. A hot accretion disk (blue ellipse) around a compact companion (cyan circle) captures part of the material (red arrows) in an outflow or Roche-lobe overflow from the primary AGB star (red circle) via two possible infall streams (dashed red/pink arrows)—these produce redshifted emission features. The accretion disk powers a fast outflow (cyan arrows) that absorbs UV photons from the disk, producing blueshifted absorption features.

size of the hot disk region must be small compared with that of the outflow.

The large observed values of the blue and red Doppler shifts of the absorption and emission features, respectively, are naturally explained in this model because both features are associated with material moving in the gravitational well of the central star near the accretion disk’s inner regions. The emission features from high-excitation lines (C IV, Si IV) are generated closer to the disk, in the infall’s hottest parts, whereas the low-excitation Mg II lines are generated in a region farther away, hence the redshift of the Mg II lines is much lower than that of the high-excitation lines.

The correlation between the variations seen in the FUV continuum and Si IV absorption line features suggests that both of these are associated with variations in the accretion rate. The mismatch between the epoch during which the Si IV(1) absorption line equivalent width peaks and that at which  $L(h)$  peaks (in exposure 50) confirms that these arise in spatially separated structures. In this model, the long-term UV and X-ray variations noted by Setal15 may result from orbital motion as varying segments of the disk are eclipsed by the AGB star.

We also find an anticorrelation between the fluxes of the C IV and Si IV emission lines—e.g., over the period covered by exposures 10–60, the Si IV flux shows a general increase, whereas the C IV flux shows a general decrease (Figure 2(b)). A plausible explanation for this anticorrelation is that it results from changes in the ionization fractions of each of these species as a function of temperature. Our simple CLOUDY (Ferland et al. 2013) modeling using uniform low-density spherical plasma clouds, with a wide range of plausible densities,  $\sim 10\text{--}10^5\text{ cm}^{-3}$ , shows that the ionization fractions of C IV and Si IV are anticorrelated for temperatures in the range  $(0.7\text{--}1.1) \times 10^5\text{ K}$ —i.e., a decrease in temperature results in an increase (decrease) in the fractional population of the

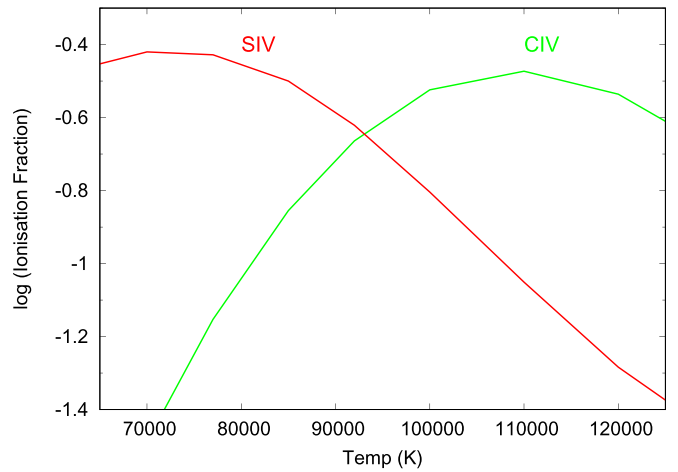


**Figure 5.** Ionization fractions of C IV (green) and Si IV (red) for a range of temperatures for a cloud of density  $10^3\text{ cm}^{-3}$ .

Si IV (C IV) ionization state (Figure 5). We note that within this temperature range, the Si IV and C IV ionization states are also well populated; they represent the second most populated states: their populations differ, at e.g.,  $T \sim 0.9 \times 10^5\text{ K}$ , by factors of 2.4 and 3.3, respectively, from that of the most populated ones.

The anticorrelation between the blueshift for the Si IV(1) absorption feature and the redshift of the Si IV(1) emission feature may be explained as follows. In our model, the P-Cygni feature is due to the sum of the features produced by (i) the absorption of continuum by the outflow and (ii) the emission from the infalling stream (which sits on top of the underlying continuum). When the outflow velocity increases, the absorption feature shifts bluewards as a whole, thus making the blue side of the emission feature stronger by decreasing the underlying absorption—the net result is that the observed redshift of the emission feature becomes smaller.

In order to explain the observed short-term variations in the line widths, red- and blueshifts, and fluxes, we propose that the infall and outflow streams experience short-term temporal variations in the densities, temperatures, velocities, and velocity gradients in these streams that are likely stochastic. The relatively large observed line widths—e.g.,  $\sim 335\text{--}515\text{ km s}^{-1}$  ( $\sim 775\text{--}1000\text{ km s}^{-1}$ ) for the emission features in Si IV(1) ( $\text{Ly}\alpha$ ), depending on the epoch, are likely a consequence of velocity gradients (due to both turbulent and systematic motion) and the presence of a range of inclinations, relative to the los, within the outflow and infall streams.

## 6. Conclusions

Using the *Hubble Space Telescope*, we have carried out UV spectroscopic observations of the late-M star, Y Gem—the most prominent member of a class of AGB stars that are sources of strong and variable UV and X-ray emission, likely resulting from accretion activity due to the presence of a binary companion.




1. Y Gem shows the presence of strong emission in the FUV ( $\sim 1120\text{--}1700\text{ \AA}$ ) and NUV ( $\sim 1600\text{--}3150\text{ \AA}$ ) bands, both in the continuum as well as in lines such as  $\text{Ly}\alpha$ , C IV  $\lambda\lambda 1548, 1551$ , Si IV  $\lambda\lambda 1394, 1403$ , and Mg II  $\lambda\lambda 2796, 2803$ .

2. The UV continuum shows short-term stochastic time variations (on timescales of  $\lesssim 20$  s); this flickering phenomenon is characteristic of the presence of an active accretion disk. We also find a long-term trend (overall decline) in the FUV continuum over a period of  $\sim 1.7$  hr.
3. The continuum can be modeled as a sum of a hotter and a cooler blackbody component. The luminosities of these components, as derived from the best-modeled pair of near-contemporaneous FUV and NUV spectra, are  $\sim 6.8 L_{\odot}$  and  $6.3 L_{\odot}$ , and the temperatures are  $\sim 3.7 \times 10^4$  K and  $\sim 10^4$  K, respectively. The changes in the FUV continuum appear to be related to similar changes in the luminosity of the hotter blackbody; the temperature is significantly less variable.
4. Neither of the two blackbodies fits the properties of a viable stellar companion (WD or main sequence) to the primary, suggesting that both the hot and cool UV components arise in the accretion disk.
5. Lines from species such as Si IV and C IV show prominent P-Cygni-type profiles, with emission and absorption features that are red- and blueshifted by  $\sim 500$  km s $^{-1}$  from the systemic velocity. The relatively large redshifts of the emission features are not consistent with a classical P-Cygni profile that results from an outflow surrounding a continuum source.
6. Our model for these (and previous) observations is that material from the primary star is gravitationally captured by a companion, producing a hot accretion disk. The latter powers a fast outflow that produces blueshifted features due to the absorption of the UV continuum emitted by the disk, whereas the redshifted emission features arise in heated infalling material from the primary.
7. The outflow velocities support a previous inference that Y Gem's companion is a low-mass main-sequence star.
8. The combined luminosity of the hot and cool blackbodies require a relatively large accretion rate,  $> 5 \times 10^{-7} M_{\odot} \text{ yr}^{-1}$ ; since the primary in Y Gem has negligible (or very weak) mass loss, wind-accretion modes are infeasible, and between CE and Roche-lobe overflow accretion modes, the latter is preferred.

We acknowledge helpful discussions with Eric Blackman related to binary accretion modes. We thank the referee, Dr. Jacco Th. van Loon, for helpful comments that helped to improve an earlier version of this paper. R.S.'s contribution to the research described here was carried out at the Jet Propulsion Laboratory, California Institute of Technology, under a contract with NASA. C.S.C. has been partially supported by the Spanish MINECO through grant AYA2016-75066-C2-1-P and by the European Research Council through ERC grant 610256: NANOCOSMOS.

J.S.F. acknowledges support from the Spanish MINECO through grant AYA2014-54348-C3-2-R. The National Radio Astronomy Observatory is a facility of the National Science Foundation operated under cooperative agreement by Associated Universities, Inc.

### ORCID iDs

R. Sahai  <https://orcid.org/0000-0002-6858-5063>  
 C. Sánchez Contreras  <https://orcid.org/0000-0002-6341-592X>  
 J. Sanz-Forcada  <https://orcid.org/0000-0002-1600-7835>

### References

- Balick, B., & Frank, A. 2002, *ARA&A*, 40, 43  
 Bruch, A. 2015, *A&A*, 579, A50  
 Castor, J. I. 1970, *MNRAS*, 149, 111  
 Chen, Z., Frank, A., Blackman, E. G., Nordhaus, J., & Carroll-Nellenback, J. 2017, *MNRAS*, 468, 4465  
 Corradi, R. L. M., Brandi, E., Ferrer, O. E., & Schwarz, H. E. 1999, *A&A*, 343, 841  
 Cox, A. N. 2000, *Allen's Astrophysical Quantities* (4th ed; New York: AIP Press)  
 Dashevsky, I., Sahu, K., & Smith, E. 2000, *Space Telescope STIS Instrument Science Report* 2000-02  
 Ferland, G. J., Porter, R. L., van Hoof, P. A. M., et al. 2013, *RMxAA*, 49, 137  
 Huarte-Espinosa, M., Carroll-Nellenback, J., Nordhaus, J., Frank, A., & Blackman, E. G. 2013, *MNRAS*, 433, 295  
 Ingleby, L., Calvet, N., Bergin, E., et al. 2009, *ApJL*, 703, L137  
 Ingleby, L., Calvet, N., Bergin, E., et al. 2011, *ApJ*, 743, 105  
 Kahane, C., & Jura, M. 1994, *A&A*, 290, 183  
 Livio, M. 1997, in *ASP Conf. Ser. 121, Accretion Phenomena and Related Outflows*, ed. D. T. Wickramasinghe, G. V. Bicknell, & L. Ferrario (San Francisco, CA: ASP), 845  
 McDonald, I., Zijlstra, A. A., & Boyer, M. L. 2012, *MNRAS*, 427, 343  
 Miller Bertolami, M. M. 2016, *A&A*, 588, A25  
 Nuñez, N. E., Nelson, T., Mukai, K., Sokoloski, J. L., & Luna, G. J. M. 2016, *ApJ*, 824, 23  
 Pronik, I. I., Merkulova, N. I., & Metik, L. P. 1999, *A&A*, 351, 21  
 Sahai, R., Findeisen, K., Gil de Paz, A., & Sánchez Contreras, C. 2008, *ApJ*, 689, 1274  
 Sahai, R., Morris, M. R., & Villar, G. G. 2011a, *AJ*, 141, 134  
 Sahai, R., Neill, J. D., Gil de Paz, A., & Sánchez Contreras, C. 2011b, *ApJL*, 740, L39  
 Sahai, R., Sanz-Forcada, J., & Sánchez Contreras, C. 2016, *JPhCS*, 728, 042003  
 Sahai, R., Sanz-Forcada, J., Sánchez Contreras, C., & Stute, M. 2015, *ApJ*, 810, 77  
 Sahai, R., & Trauger, J. T. 1998, *AJ*, 116, 1357  
 Sánchez Contreras, C., & Sahai, R. 2001, *ApJL*, 553, L173  
 Snaid, S., Zijlstra, A. A., McDonald, I., et al. 2018, *MNRAS*, 477, 4200  
 van der Klis, M. 2006, in *Compact Stellar X-ray Sources* (Cambridge: Cambridge Univ. Press), 39  
 van Leeuwen, F. 2007, *A&A*, 474, 653  
 van Loon, J. T., Kaper, L., & Hammerschlag-Hensberge, G. 2001, *A&A*, 375, 498  
 Yang, H., Linsky, J. L., & France, K. 2011, *ApJL*, 730, L10  
 Zamanov, R. K., Boeva, S., Nikolov, Y. M., et al. 2017, *AN*, 338, 680